

# The Three-Dimensional Expansion of the Ejecta from Tycho's Supernova Remnant

Brian J. Williams,<sup>1,2</sup> Nina M. Coyle,<sup>2,3</sup> Hiroya Yamaguchi,<sup>2,4</sup> Joseph Depasquale,<sup>1,5</sup> Ivo R. Seitzzahl,<sup>6,7</sup> John W. Hewitt,<sup>8</sup> John M. Blondin,<sup>9</sup> Kazimierz J. Borkowski,<sup>9</sup> Parviz Ghavamian,<sup>10</sup>  
Robert Petre,<sup>2</sup> Stephen P. Reynolds,<sup>9</sup>

Received \_\_\_\_\_; accepted \_\_\_\_\_

---

<sup>1</sup>Space Telescope Science Institute, Baltimore, MD 21218; bwilliams@stsci.edu

<sup>2</sup>NASA Goddard Space Flight Center, X-ray Astrophysics Laboratory, Greenbelt, MD 20771, USA

<sup>3</sup>University of Chicago, Department of Physics, Chicago, Illinois 60637

<sup>4</sup>CRESST/University of Maryland, College Park, College Park, MD 20742

<sup>5</sup>Harvard-Smithsonian Center for Astrophysics, Cambridge, MA 02138

<sup>6</sup>School of Physical, Environmental and Mathematical Sciences, University of New South Wales, Australian Defence Force Academy, Canberra, ACT 2600, Australia

<sup>7</sup>Research School of Astronomy and Astrophysics, Australian National University, Canberra, ACT 2611, Australia

<sup>8</sup>University of North Florida, Department of Physics, 1 UNF Drive, Jacksonville, FL 32224, USA

<sup>9</sup>Department of Physics, North Carolina State University, Raleigh, NC 27695

<sup>10</sup>Department of Physics, Astronomy, and Geosciences, Towson University, Towson, MD 21252

## ABSTRACT

We present the first three-dimensional measurements of the velocity of various ejecta knots in Tycho’s supernova remnant, known to result from a Type Ia explosion. Chandra X-ray observations over a 12-year baseline from 2003 to 2015 allow us to measure the proper motion of nearly 60 “tufts” of Si-rich ejecta, giving us the velocity in the plane of the sky. For the line of sight velocity, we use two different methods: a non-equilibrium ionization model fit to the strong Si and S lines in the 1.2-2.8 keV regime, and a fit consisting of a series of Gaussian lines. These methods give consistent results, allowing us to determine the red or blue shift of each of the knots. Assuming a distance of 3.5 kpc, we find total velocities that range from 2400 to 6600 km s<sup>-1</sup>, with a mean of 4430 km s<sup>-1</sup>. We find several regions where the ejecta knots have overtaken the forward shock. These regions have proper motions in excess of 6000 km s<sup>-1</sup>. Some Type Ia supernova explosion models predict a velocity asymmetry in the ejecta. We find no such velocity asymmetries in Tycho, and discuss our findings in light of various explosion models, favoring those delayed detonation models with relatively vigorous and symmetrical deflagrations. Finally, we compare measurements with models of the remnant’s evolution that include both smooth and clumpy ejecta profiles, finding that both ejecta profiles can be accommodated by the observations.

## 1. Introduction

Tycho’s supernova remnant (SNR; hereafter Tycho) is the remnant of the supernova (SN) first observed in 1572 CE (Stephenson & Green 2002). It was classified by Baade (1945) as a “Type I” event, and an analysis of the X-ray emitting ejecta suggested a “normal” Type Ia SN event (Badenes et al. 2006). This was confirmed via detection and spectroscopy of light echoes

by Rest et al. (2008) and Krause et al. (2008). These SNe are generally believed to result from a thermonuclear explosion of a white dwarf in a binary system, destabilized by mass transfer. While the nature of the binary companion is unclear, there are two leading scenarios: the single-degenerate (SD) model, in which a white dwarf accretes matter from a non-degenerate companion, exploding when it reaches the Chandrasekhar limit of  $\sim 1.4 M_{\odot}$  (Whelan & Iben 1973); and the broadly defined double-degenerate (DD) model, which consists of an explosion triggered by the merging of two white dwarfs by various means (Webbink 1984).

In an earlier work (Williams et al. 2013, hereafter “Paper I”), we examined *Spitzer* infrared (IR) observations of the remnant, which show emission from interstellar dust grains, warmed in the post-shock environment by collisions with energetic electrons and ions. We fit models to the IR colors that allowed us to determine the post-shock gas density, which we found to vary as a function of azimuthal angle around the shell, with densities in the east and northeast higher by a factor of several than those in the west and southwest.

In a subsequent work (Williams et al. 2016, hereafter “Paper II”), we examined the proper motions of the forward shock in both X-rays and radio. The emission processes in these two wavebands are the same: nonthermal synchrotron radiation resulting from relativistic electrons, accelerated by the amplified magnetic fields (Ressler et al. 2014; Tran et al. 2015) in the forward shock wave from the supernova. We used *Karl G. Jansky Very Large Array (VLA)* radio observations spread over 30 years and *Chandra* X-ray observations spread over 15 years to measure the expansion rate of the remnant at  $\sim 20$  locations around the shell, finding that the velocity of the forward shock varies by roughly a factor of two from one side of the shell to the other. The direction of the velocity asymmetry is such that the fastest shocks propagate into the lowest density environments determined in Paper I, as expected.

The simplest explanation for this is that Tycho’s SNR is expanding into a non-uniform interstellar medium (ISM), such as a pre-existing density gradient. However, another intriguing

possibility is that the explosion itself was non-uniform. The explosion mechanism for Type Ia SNe is poorly understood, but there have been hints that at least some explosions may be asymmetric. Supernovae themselves are unresolvable, but spectroscopic information embedded in the emission lines during the nebular phase has shown evidence in some SNe Ia for the red and blueshifted ejecta velocities to be different (Motohara et al. 2006; Maeda et al. 2010). Wang & Wheeler (2008) summarize evidence for optical polarization in spectral lines in some SNe Ia before maximum, indicating significant asymmetry. From the SNR side, there is evidence for an asymmetric distribution of ejecta in the Type Ia SNRs G1.9+0.3 (Borkowski et al. 2017) and SN 1006 (Winkler et al. 2014), but these are based only on the spatial distribution, not the dynamic motions of the ejecta. Although there is evidence for local asymmetry in Tycho (Yamaguchi et al. 2017), the global ejecta distribution has not been investigated.

**Previous studies by Furuzawa et al. (2009) and Hayato et al. (2010) examined the doppler broadening of the Fe and intermediate-mass elements within the ejecta, finding that the Si, S, and Ar expand at a higher velocity than the Fe. Katsuda et al. (2010) examined the proper motions of the outer ejecta in five large ( $\sim$  arcminute scale) regions around the periphery of Tycho, finding an average expansion rate of  $0.294'' \text{ yr}^{-1}$ .** In a recent paper by Sato & Hughes 2016, hereafter SH16, the authors looked at several “blobs” of ejecta in Tycho’s SNR, identifying both red and blueshifted velocity components from the Doppler shifts of the spectral lines in a deep (750 ks) 2009 *Chandra* observation of Tycho. They find Doppler velocities in excess of  $5000 \text{ km s}^{-1}$  along the line of sight for ejecta blobs near the center of the remnant moving both towards and away from the observer. Their work represents the first direct ejecta velocity measurements along a line of sight direction in Tycho’s SNR.

In this work, we build upon the work of SH16 by extending the ejecta velocity measurements to all three dimensions, building up a velocity-vector map of nearly 60 spatially-coherent ejecta knots, roughly evenly distributed throughout the remnant. The fluffy interior of Tycho is

dominated by emission from the ejecta, most prominently the Si and S lines at  $\sim 1.86$  and  $\sim 2.45$  keV, respectively (Warren et al. 2005). We combine line-of-sight (LOS) velocities measured from the Doppler shifts of these spectral lines in each of these knots with their proper motion in the plane of the sky, as measured from observations in 2003 and 2015. With velocities in all three dimensions, we derive absolute magnitudes and directions of the velocity vectors of the ejecta knots, and show that the ejecta velocities are consistent with a symmetric explosion. Similar work has been done for core-collapse SNRs, such as Cas A (Fesen et al. 2006; Delaney et al. 2010), but this work represents the first such map of a Type Ia SNR.

## 2. Observations

Tycho has been observed a total of five times with *Chandra*. A 50 ks observation in 2000 used the ACIS-S3 chip, which is not quite large enough to fit the entire remnant on it. As a result, about 25% of the remnant, along the southern shell, is cut off by the chip edge (Hwang et al. 2002). The next four observations (150 ks in 2003 and 2007, 750 ks in 2009, and 150 ks in 2015) all used the ACIS I-array and cover the entire remnant. The choice of data sets that we use for this work depends on whether we are measuring the proper motion or the LOS velocity. For our proper motion measurements, we desire the longest baseline possible with the same instrument, so we make our measurements on the 2003 (PI: J.P. Hughes) and 2015 (PI: B.J. Williams) data. Additional factors for this decision are that the 2003 exposure is much deeper than the 2000 exposure, the 2015 observation was specifically planned to match that from 2003, and the 2003 image covers the entire remnant, while the 2000 image cuts off the southern portion of the remnant.

The 2003 observation was taken in a single pointing beginning on 2003 Apr 29, while the 2015 observation was also taken in a single pointing beginning on 2015 Apr 22, a time baseline of 12.0 yr. We follow an identical data reduction process as that described in Paper II, which is

based on the work of Katsuda et al. (2010), where we use version 4.7 of CIAO and version 4.6.5 of CALDB to process all epochs. We found no significant background flaring in the light curves. We align all epochs to a common reference frame (the deep 2009 observation is used as the relative reference frame) using detected point sources in the field of view. The images are slightly smoothed using a 2-pixel Gaussian, which has virtually no effect on the profile shapes described in Section 3, but does significantly decrease the pixel-to-pixel Poisson noise level.

Our spectral analysis of each region is performed entirely using the 2009 observation (PI: J.P. Hughes), which was split into nine different segments between 2009 Apr 13 and 2009 May 3 with an effective total exposure time of 734 ks. We follow a procedure used in Winkler et al. (2014), similar to that of SH16, stacking spectra for a given region from all nine observations, using the *specextract* tool in CIAO, weighting spectral files and response files appropriately. Spectral fits were performed using XSPEC version 12.9.0p, which contains version 3.0 of AtomDB.

Our choice of knots for both spectral extraction and proper motion measurement was guided by several requirements. First and most importantly, we searched the entire remnant in both the 2003 and 2015 epochs for any structure that maintained a coherent shape between both epochs *and* had a proper motion detectable by eye. This limited us to regions away from the center of the remnant, as the ejecta velocities there are mostly along the LOS. This is not a loss, though, as these regions in the center of the remnant have been studied by SH16. Secondly, we ensured that the knots were bright enough to get a good signal-to-noise for the spectral fitting. This was the easiest qualification to meet; we required a minimum of 5000 counts in a given spectrum, but most of our regions have easily over 10,000, thanks to the depth of the 2009 observation. Thirdly, we ensured that the 1D profiles that we extracted, described below, have a constant shape at the leading edge of the emission. This was done to avoid the situation that we encountered a few times in Paper II, where the shape of the emission profile changed between the two epochs. Finally, we attempted to find knots that were roughly evenly distributed in all sectors of Tycho. In

some places, this was harder than others; the eastern and southeastern portions of the interior of the remnant were particularly difficult. The issue was not in finding knots bright enough, but in finding knots that maintained spatial coherence between the two epochs.

We emphasize that it is neither within the scope of this paper nor is it feasible to account for the motion of every tiny structure within the remnant. We ended up with a total of 57 ejecta knots that satisfied all of our conditions, above. These regions are shown in Figure 1. **For each of the knots, we drew an extraction region centered on the brightest part of the knot, with the region cutting off when the flux (as determined from the exposure-corrected 2009 flux image) dropped below  $1.5 \times 10^{-7}$  photons  $\text{cm}^{-2} \text{s}^{-1}$ .** We used that exact region for the spectral extraction, using an off-source background from an annulus surrounding the remnant. We experimented with other choices of off-source background selection, but found no difference in the resulting spectral fits (the background accounts for, on average, about 0.5% of the flux in the 1.2–2.8 keV band that we use for our fitting). **We also experimented with local backgrounds from within the remnant surrounding each knot. We find, as reported in SH16, that the local backgrounds vary significantly enough that there is no way to know what an accurate local background is. Choosing these local backgrounds increases the velocities we measure (in both directions: redshifts get redder and blueshifts get bluer), but in approximately equal amounts of around  $1000 \text{ km s}^{-1}$ .** Given the uncertainties of determining the appropriate local background for each individual knot, we have stayed with the systematic approach of using a uniform off-source background to be the safest and most conservative approach. To measure the proper motion, we used a “projection” region in ds9, drawn along both the X and Y directions.

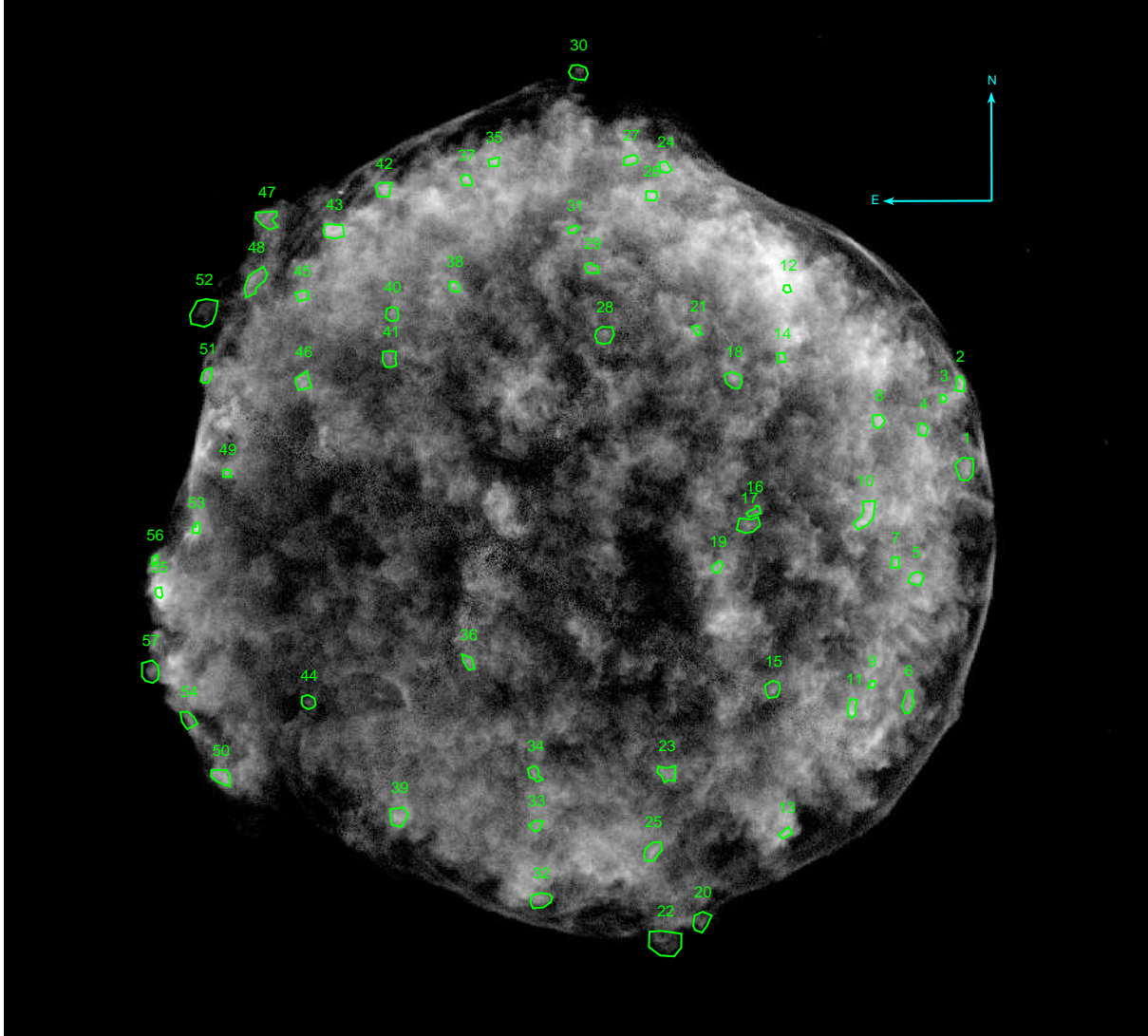


Fig. 1.— A broadband (1-8 keV) *Chandra* image, overlaid with the 57 regions used for the expansion measurements. Tycho’s SNR is  $\sim 8.5'$  in diameter.

## 2.1. ACIS-I Gain Calibration

Measuring the velocity along the line of sight is done by measuring the red and blueshifts of the Si and S lines that dominate the spectra. We detail in Section 3 how this was done, and detail the statistical uncertainties of these measurements. We discuss here the systematic

uncertainty introduced by the accuracy of *Chandra*'s gain calibration. To better understand this, we consulted with *Chandra* calibration experts, who assisted us in quantifying this (P. Plucinsky and N. Durham, private communication).

The gain for the ACIS-I instrument is calibrated using three onboard sources with spectral lines at known energies: an Al  $K\alpha$  line at 1.487 keV, a Ti  $K\alpha$  line at 4.511 keV, and a Mn  $K\alpha$  line at 5.898 keV. The *Chandra* calibration team went back to these 2009 observations and compared the measured line energies for all three of these lines for the entire ACIS-I array. The focal plane temperature (which can affect the gain) was stable during these observations. They found that for virtually the entire ACIS-I array, the gain calibration is good to a level of  $<0.3\%$ , with some places being significantly better, particularly for the Ti and Mn  $K\alpha$  lines. However, because our measured lines of Si and S lie closer to the Al  $K\alpha$  calibration line, we adopt the conservative systematic uncertainty of  $0.3\%$ , or  $900 \text{ km s}^{-1}$  for our line of sight ( $V_z$ ) velocities.

The exceptions to this are the center rows of all 4 ACIS-I chips, where the calibration is worse for the Al  $K\alpha$  line in particular. In some places, the measured values of the calibration lines differ by up to  $1\%$  from the fiducial values. The 2009 observation, like most *Chandra* observations of Tycho, used the ACIS-I array, centered on the approximate center of the remnant. Because of this, most of the remnant *does not* fall on the centers of the four chips. To check whether any of our regions fell in the “bad” calibration regions, we generated an image of the remnant containing only the center rows in which the calibration uncertainty was greater than  $0.3\%$ . We then overplotted our regions, and found that only four of them (regions 24, 26, 27, and 30) lie within the affected rows. This is shown in Figure 2. We still report measured values for those four regions, but we note that the uncertainty could be as high as  $1\%$ , or  $3000 \text{ km s}^{-1}$ .

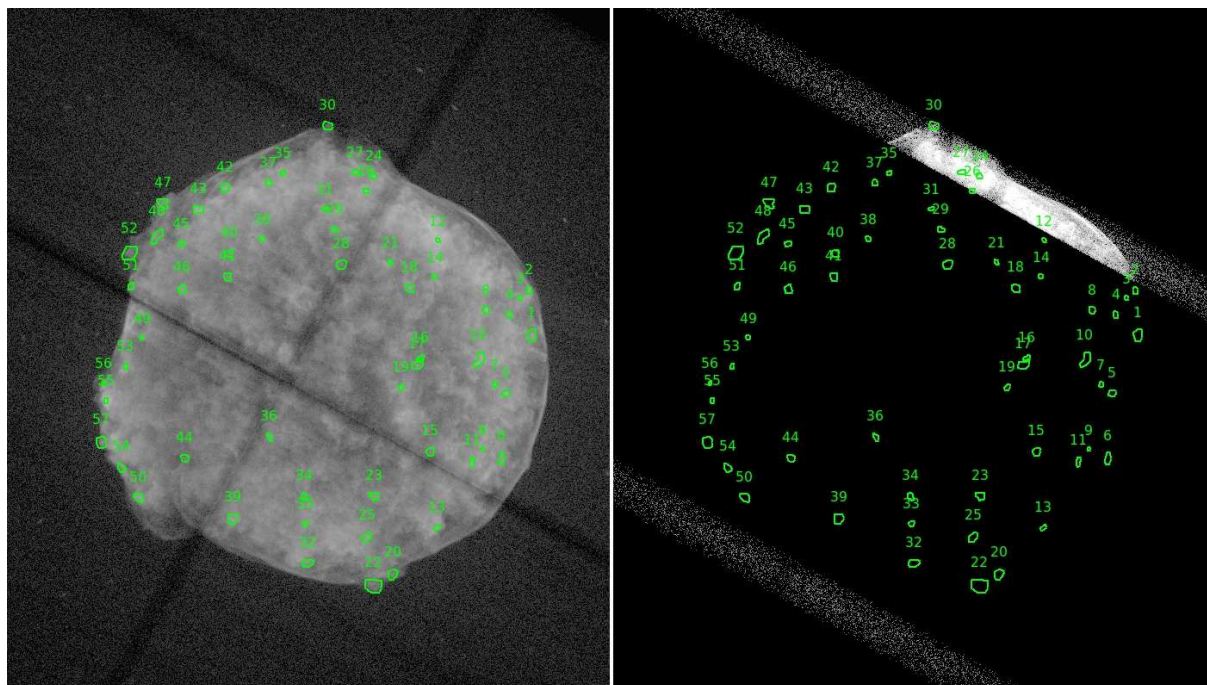


Fig. 2.— *Left*: the events file for the merged 2009 ACIS-I observation, overplotted with our measurement regions, shown for reference. *Right*: The events file with only the chip rows that fall outside of a calibration range of 0.3%, overplotted with the same regions.

### 3. Measurements

#### 3.1. Proper Motions

Our procedure for measuring the proper motions follows that of Paper II, which is based on Katsuda et al. (2008) and used in other SNR works, such as Winkler et al. (2014) and Yamaguchi et al. (2016). We extract the 1D radial profiles from both epochs in both the X and Y (R.A. and Dec.) directions, with uncertainties (where the uncertainty on each pixel is the square root of the number of counts in that pixel, which is summed across the width of the projection region), and shift epoch 1 relative to epoch 2. We extract the profiles in pixel space, with shifts calculated on a grid of 2000 points with a size of 0.025 pixels. A fit is obtained when the value of  $\chi^2$  is minimized, and the 90% uncertainties we report in Table 1 come from a shift in  $\chi^2$  of 2.71

in either direction. As in Paper II, we fit for the shift in an area containing the leading edge of the filament. **We show the X and Y projections from several sample regions in Figure 3. Regions that maintain their shape particularly well have very small errors; in some cases, less than  $10 \text{ km s}^{-1}$ .**

Converting a measured proper motion to an absolute velocity requires knowing the distance to the remnant. The reported value of the distance to Tycho has varied in the literature over time. An analysis by Chevalier et al. (1980) suggested a distance of 2.3 kpc, a similar distance to that reported in Albinson et al. (1986). Later work by Schwarz et al. (1995) favored a distance of over 4 kpc. In Paper I, we compared hydrodynamic simulations to the observations, preferring a distance of 3.5 kpc, a distance that fits nicely with the 3.8 kpc recently derived by SH16. For the purposes of this paper, we adopt a distance of 3.5 kpc, and scale proper motion velocities accordingly, noting that the results of this paper are not dependent on knowing the absolute distance. The proper motions for our 57 regions are listed in Table 1. As expected, higher values for the proper motion are found in the regions along the edge of the remnant, while lower ones are found for those closer to the interior. In several regions where the ejecta are clearly seen in the image to be protruding in front of the nonthermal rim (e.g., regions 22, 30, and 57), we measure proper motion velocities in excess of  $6000 \text{ km s}^{-1}$ . **In Figure 4, we show the radial velocities in the plane of the sky (i.e., the combined X and Y velocities) as a function of their radial distance from the presumed explosion site that we found in Paper II ( $\alpha = 0^h 25^m 22.6^s$  and  $\delta = 64^\circ 8' 32.7''$ ).**

**This choice of explosion site is offset by about  $23''$  from the geometric center of the remnant. The choice of this explosion site versus the geometric center of Ruiz-Lapuente et al. (2004) has little effect on the radii and deceleration parameters measured. Along regions located in the SE and NW portions, the effect is nearly zero, while the most affected region, region 19, differs by about 20%. The average effect is  $\sim 9\%$ .**

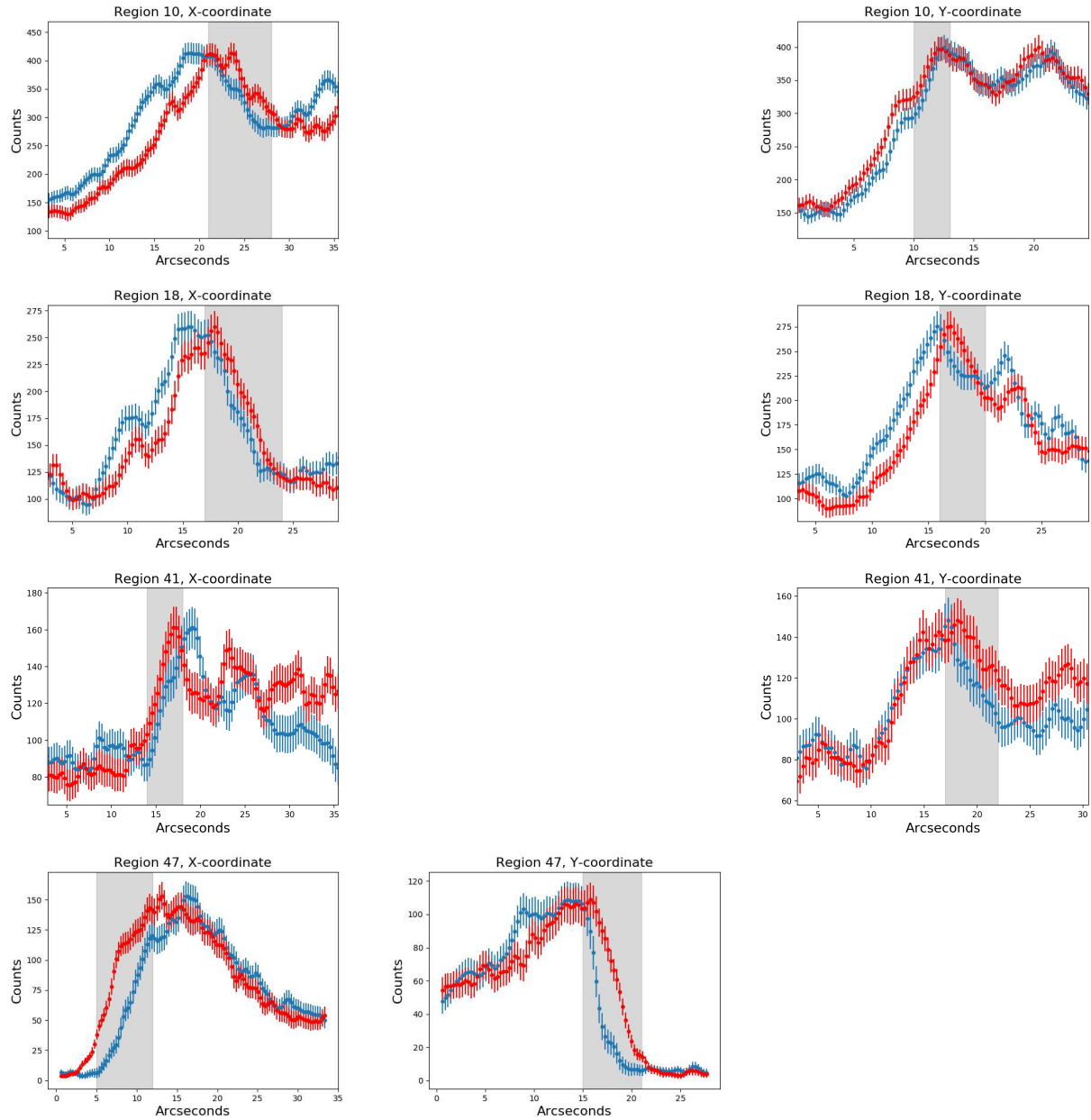


Fig. 3.— An example of our 1D profiles from several sample regions. We fit the leading edge of the emission, shifting epoch 1 (blue profile) to fit epoch 2 (red) in the region containing the leading edge of the emission in epoch 2 (grey region).

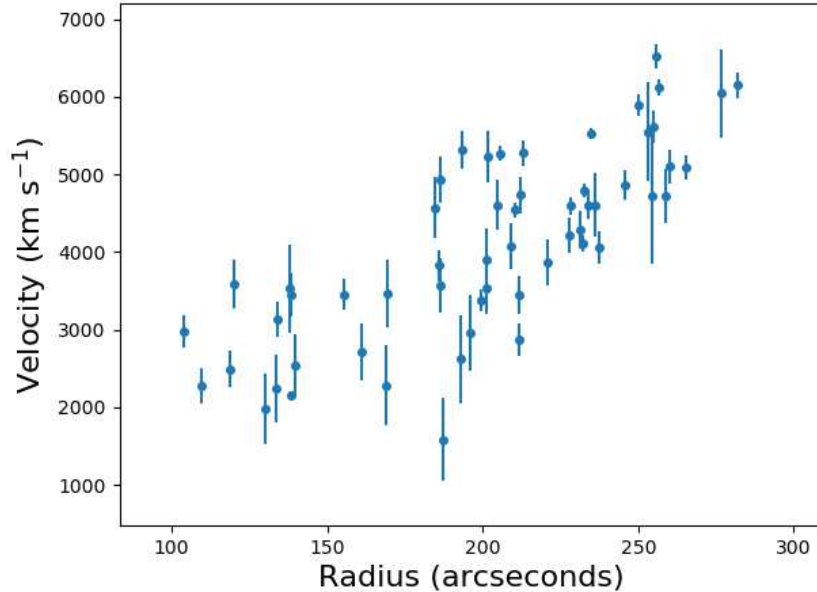


Fig. 4.— Total velocity in the plane of the sky plotted against the radius from the explosion site, as described in the text. The radius depends slightly on the choice of explosion site (see description in the text), though the velocity is independent of this and only depends on the measured proper motions, known time baseline, and the assumed distance of 3.5 kpc.

### 3.2. Doppler Velocities

While the proper motion measurements can give us a velocity in the plane of the sky (modulo the distance to the remnant), the LOS velocity is needed for a total spatial velocity of any particular ejecta knot. SH16 looked at the doppler shifts of several “blobs” of ejecta in Tycho, mostly in the center of the remnant, and converted these doppler shifts to a spatial velocity. We follow a similar procedure here, applying it to our regions, which are outside the center of the remnant, and thus can be combined with the measured proper motions.

The ejecta emission from Tycho is dominated by remarkably strong emission from the Si XIII  $K\alpha$  line at around 1.85 keV, a line commonly seen in young Type Ia SNRs. Another strong

line from S XV is present at about 2.45 keV, and weaker lines from Mg, Ar, Ca, and Fe are also present in the spectrum. We focus here on the energy range from 1.2–2.8 keV, where the Mg, Si, and S lines appear. We use two independent procedures to determine the red/blueshift of each of our 57 regions using this energy range. For one method, used in SH16, we fit a non-equilibrium ionization (NEI) model to the spectrum, modeling the temperature and ionization state of the plasma and fitting an overall red/blueshift to the entire spectrum. As an alternative check, we fit Gaussian line profiles to each of the lines in the spectrum, fitting the centroid, and thus the doppler shift, of *only* the Si K $\alpha$  line.

In modeling the spectrum with a thermal model, we use an absorbed NEI model with an underlying power-law component to account for the possibility of any non-thermal emission that might be present along the line of sight. We fix the absorbing column density at  $6 \times 10^{21} \text{ cm}^{-2}$ , consistent with the values reported in Hwang et al. (2002) and SH16, but we note that the exact value of this parameter (within the reasonable range as reported in the literature of  $5 - 10 \times 10^{21} \text{ cm}^{-2}$ ) has no effect on the fits. We also fix the value of the power-law index to 2.6, consistent with the values found in Cassam-Chenaï et al. (2007) and Tran et al. (2015). This value also has no effect on the fits, as in almost all of our 57 cases, the normalization of the power-law component simply drops to zero, as expected for emission in the interior of the remnant. Nonetheless, we keep this component in for completeness. In the NEI model, the temperature and ionization timescale ( $\tau_i \equiv \int_0^t n_e dt$ ) are allowed to vary freely, as are the abundances of Mg, Si, and S. We fit for the doppler shift of the NEI model, as a whole, and convert this to a velocity. The uncertainties we report are the 90% confidence intervals for the value of the redshift. We list the fit parameters of the NEI model in Table 2.

As a check on these numbers, we apply a different model, consisting of Gaussian lines for the Mg, Si, and S lines, on top of an absorbed thermal bremsstrahlung model with an underlying power-law component. The absorbing column density and power-law index are fixed to those

above, while the temperature of the thermal continuum is fixed to 1 keV. In order to translate a measured line centroid into a doppler velocity shift, we first need to determine the rest energy of the Si  $K\alpha$  line, which has a dependency on temperature and ionization state. The emission from Si in Tycho is somewhat complicated and consists of emission from both H and He-like states. The dominant line around 1.85 keV is actually a triplet, consisting of a resonance line with a rest energy of 1.865 keV, an intercombination line, with a rest energy of 1.854 keV (actually, this line itself is a doublet, but the lines are so close as to essentially be one line), and a forbidden line, with a rest energy of 1.840 keV.

These lines are not resolvable with CCD spectrometers such as those on *Chandra*, and thus blend into one line, which we refer to here as the Si  $K\alpha$  line. Additionally, two other lines from the  $K\beta$  and  $K\gamma$  transitions occur at 2.183 and 2.294 keV, respectively. Finally, a  $Ly\alpha$  line from Si XIV appears at 2.006 keV, which blends with the Si  $K\alpha$  line. While it cannot be resolved from the  $K\alpha$  line, the  $Ly\alpha$  line can be seen as an asymmetric “tail” on the blue side of the  $K\alpha$  line.

Our model for these lines consists of seven Gaussian components on top of the thermal bremsstrahlung and power-law components. The seven components correspond to the Si  $K\alpha$ ,  $K\beta$ ,  $K\gamma$ , and  $Ly\alpha$  lines, as well as one component for the Mg  $K\alpha$  line at  $\sim 1.35$  keV, and two more for the  $K\alpha$  and  $Ly\alpha$  lines of S at 2.45 and 2.62 keV, respectively. In general, the line centroids are allowed to float freely, with the caveats that the Si  $K\gamma$  line is fixed to a centroid that is 0.111 keV higher than the  $K\beta$  line, and the line widths for all Si species are tied together (as are those for S).

From the theoretical side, we calculated the centroid of the Si  $K\alpha$  line on a two-dimensional grid in temperature and ionization timescale parameter space. From our NEI model fits to each region, we find that the temperature ranges from 0.57 to 2.61 keV, while the ionization timescale varies from  $\sim 2 \times 10^{10} - 1 \times 10^{12}$   $\text{cm}^{-3}$  s, though most values fall in a much smaller range of  $4 \times 10^{10} - 2 \times 10^{11}$   $\text{cm}^{-3}$  s. Nonetheless, if we take the most extreme values for both quantities, we find that the Si  $K\alpha$  centroid varies over only a small range, from 1.8558 to 1.8582 keV, with

an average value of 1.8570 keV. We use this value as the “fixed” rest energy, noting that the systematic uncertainties in either direction are 1.2 eV, or 190 km s<sup>-1</sup>, significantly smaller than the statistical errors on the NEI fits, above.

The Si Ly $\alpha$  line at 2.006 keV is not affected by temperature or ionization state, so its shift will *only* be affected by the doppler shift resulting from the LOS velocity of each ejecta knot. In principle, an accurate determination of the Ly $\alpha$  line centroid could solely be used to measure the doppler velocity, but this would require an X-ray micro-calorimeter with high spectral and spatial resolution. While we cannot, using CCD spectra, accurately determine the Ly $\alpha$  centroid, we do fix it in the model to a value of 0.149 keV (2.006 - 1.857 keV) higher than that of Si K $\alpha$ , forcing these two lines to move together. We fit the same 1.2–2.8 keV energy range as before. The fits are statistically better for this model, but this is expected, given the increased number of free parameters within the model.

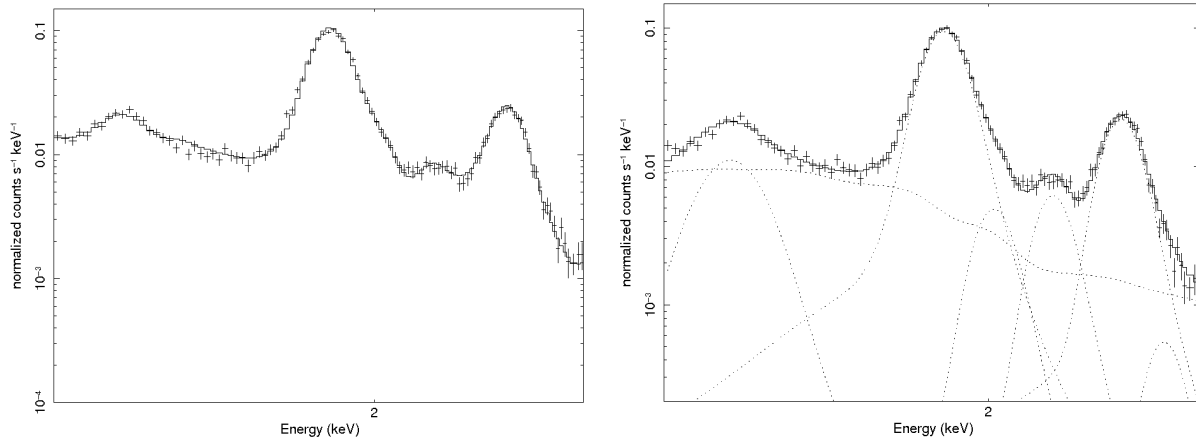


Fig. 5.— *Left*: The 1.2–2.8 keV spectrum from region 46, fit with the NEI thermal model described in the text. *Right*: The same data, but fit with the Gaussian line model described in the text. The continuum is a thermal bremsstrahlung model with temperature fixed to 1 keV. From left to right, the lines are Mg K $\alpha$ , Si K $\alpha$ , Si Ly $\alpha$ , Si K $\beta$ , S K $\alpha$ , and S Ly $\alpha$ .

In 52 out of our 57 regions, the value for the red/blueshift of the Si K $\alpha$  line using this

Gaussian line method agrees within errors of that measured from the NEI model fit. Even in the other five, the values are not significantly different, but fall just outside of the range of uncertainties. That these two different methods agree so well increases our confidence in the robustness of our NEI model fits, and we report the velocities measured from that model in Table 1. We show an example of both an NEI model fit and a Gaussian line model fit to one of our regions, region 46, in Figure 5. As expected, the doppler velocities are lower than those reported in SH16, since their numbers come mostly from ejecta knots near the center of the remnant, while ours come from the outer portions. We find a wide range of both redshifted and blueshifted velocities, ranging from 320 to 3360 km s<sup>-1</sup>. Even though our regions were chosen blindly, with no *a priori* knowledge of the doppler shift in a given ejecta knot, we find roughly equal numbers of red and blueshifted knots (30 red, 27 blue). **As shown in Figure 6, the redshifted and blueshifted knots are roughly evenly distributed throughout the remnant, and in some cases, knots in relatively close spatial proximity are moving in different directions. SH16 show a similar figure in their work, except that their regions are in the center of the remnant.**

### 3.3. Total Velocities

With the proper motion and LOS velocities calculated for all 57 of our regions, we can construct total velocity vectors for each where both the magnitude and direction are known. We report the total velocities and their components in Table 1. For the velocity components, we use a Cartesian coordinate system, where the X-Y plane corresponds to the plane of the sky, with X-positive to the right (west) and Y-positive in the up (north) direction. The Z-axis is positive moving away from the observer (redshift) and negative towards the observer (blueshift). We find total velocities that range from just under 2400 km s<sup>-1</sup> to nearly 6600 km s<sup>-1</sup>, with mean and median values of 4430 and 4450 km s<sup>-1</sup>, respectively. **This is quite close to the value of 4700 km s<sup>-1</sup> found by Hayato et al. (2010).**

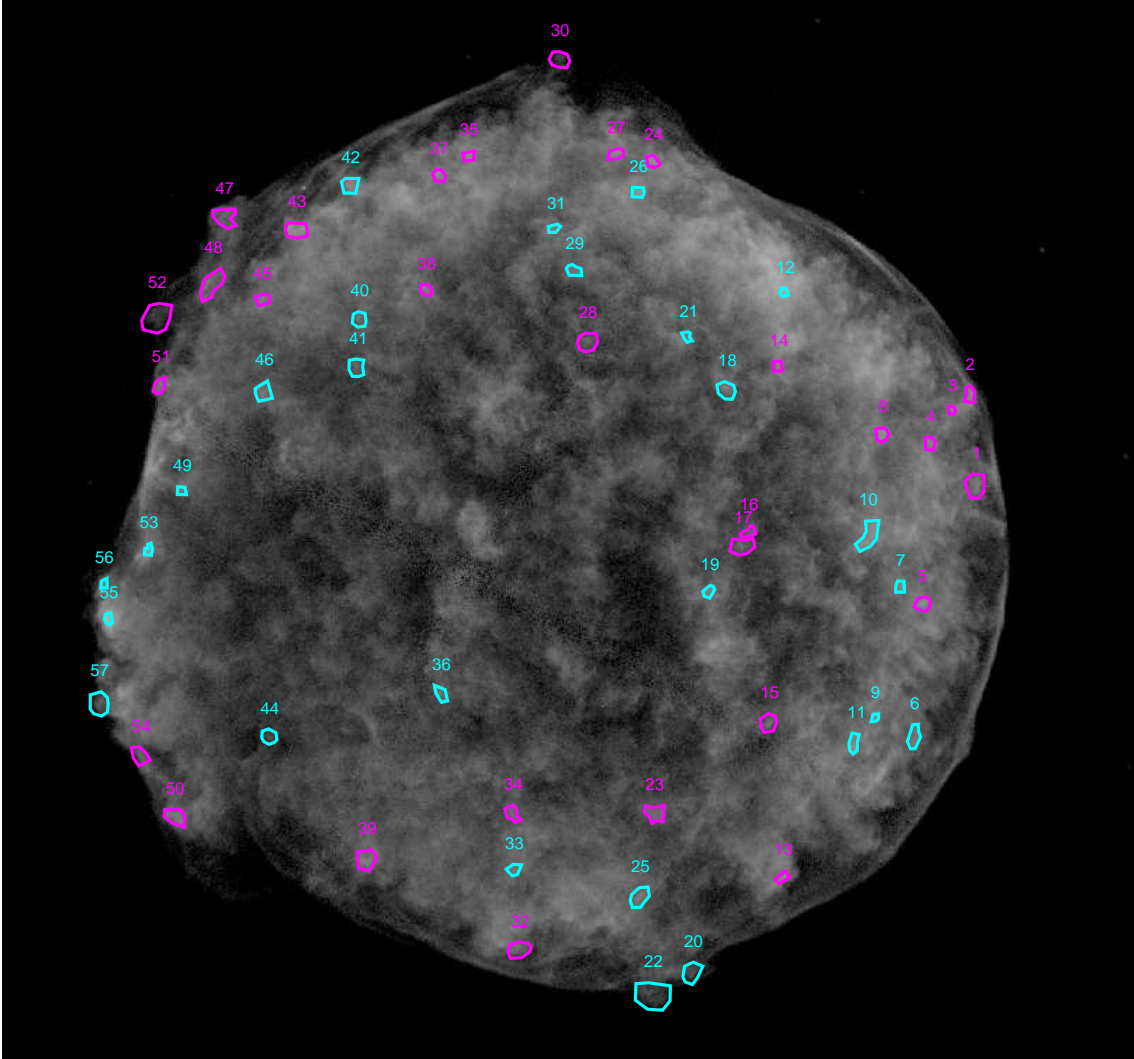


Fig. 6.— This is identical to Figure 1, except that the regions have been color-coded magenta and cyan to indicate whether the knot is redshifted or blueshifted, respectively.

To construct a velocity vector for each knot for display purposes, one must know the position of the knot within the remnant. While the X and Y positions simply correspond to the R.A. and Dec. of the knots' coordinates, there is no inherent way of knowing the Z-coordinate. Still, we can make some reasonable assumptions. The knots should move radially from the explosion site out, and we assume that Tycho is spherically symmetric with a radius of 4.33 pc (4.2' at 3.5 kpc). The latter is reasonably well justified by noting the near-perfect circular shape of the remnant on

they sky (while it is possible that the remnant has the shape of, e.g., a prolate spheroid viewed “end-on,” this requires our position to be coincidentally located along the major axis, which is unlikely), as well as by the fact that our proper motion velocities at the extreme edge of the remnant are quite well matched to the doppler shifted velocities of the knots in the center of the remnant as measured by SH16. We therefore assume that the Z position is simply the Z-velocity multiplied by the age of the remnant (437 yr in the 2009 epoch), normalized to the highest proper motion value we measure ( $6517 \text{ km s}^{-1}$ ). For example, whatever its X and Y coordinates, a knot with a redshift of  $3260 \text{ km s}^{-1}$  would be halfway between the center of the remnant and the far edge of the shell.

#### 4. Discussion

Quantitatively speaking, we can average the velocities in the X, Y, and Z directions. We account for the selection effect of the location of the blobs by weighting the averages to account for the number of blobs present in, for example, the positive and negative X-coordinate (the right and left halves of the remnant). We find average velocities of  $-179$ ,  $-88$ , and  $83 \text{ km s}^{-1}$  in the X, Y, and Z directions, respectively. These are negligible compared to the magnitudes of the velocity vectors themselves. We can further quantify this by making histograms of the velocity distribution of the knots in each direction. We show these in Figure 7. The limited number of knots forces us to use relatively large velocity bins of  $\sim 2000 \text{ km s}^{-1}$  for these plots; nonetheless, the distributions around zero are fairly symmetric even with such coarse bins. The Z-distribution has a minimum around zero because the only knots that would have exactly zero velocity in the Z-direction are those along the outermost periphery of the remnant (i.e., moving entirely in the plane of the sky), and we have relatively few of those. We see no evidence for an asymmetric expansion of the ejecta in Tycho.

It is interesting to note the difference between the expansion of the ejecta, which appears

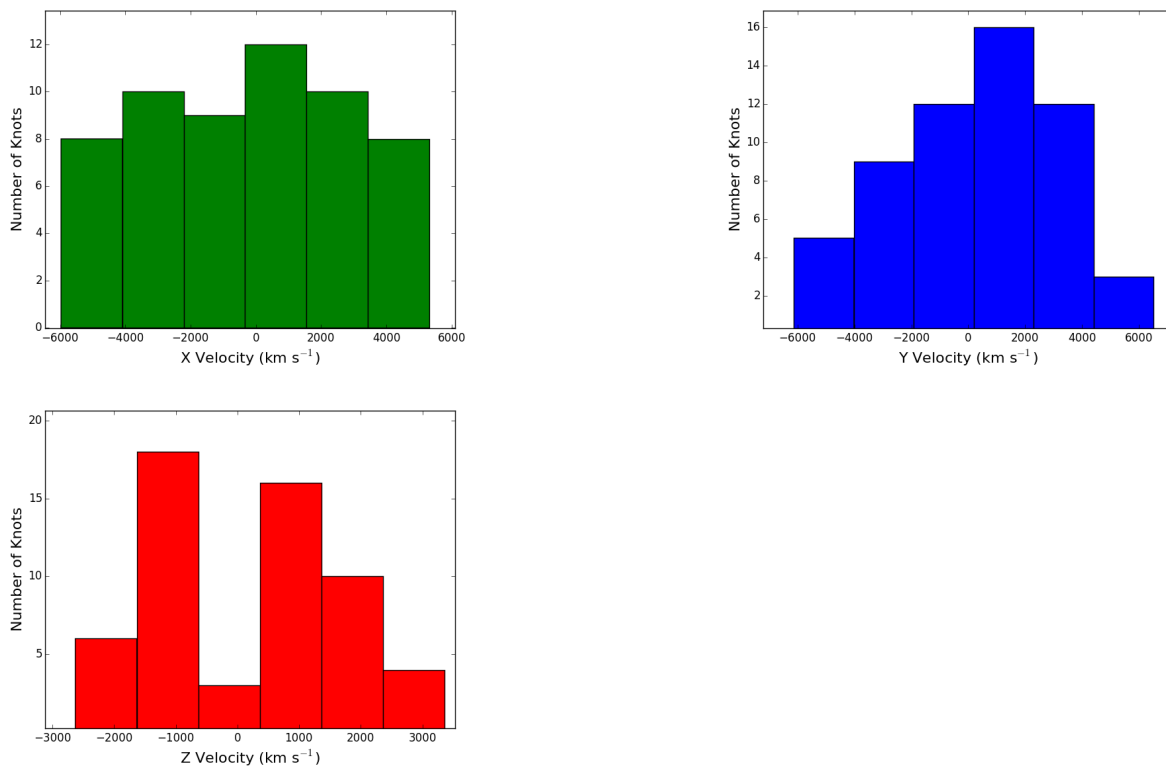


Fig. 7.— Histograms of the velocity distribution in the X (green), Y (blue) and Z (red) directions.

symmetric, and the expansion of the forward shock wave, delineated by synchrotron emission surrounding the periphery of Tycho. In Paper II, we show that the forward shock is expanding significantly faster in the western hemisphere than in the east (and particularly northeast). We interpreted this, along with our results from Paper I, as evidence for a density gradient in the ISM that has begun to slow the blast wave in the eastern portions of the remnant. Likely due to their high density contrast, the clumps of ejecta that we measure here have not yet been significantly decelerated by the more dense material on the east and northeast sides of the remnant.

We can also examine the spatial distribution of the Si, though only in the plane of the sky. In Figure 8, we show an equivalent width map of the Si-rich ejecta. We follow the procedure laid out in Winkler et al. (2014), where maps like this were created for SN 1006. The equivalent

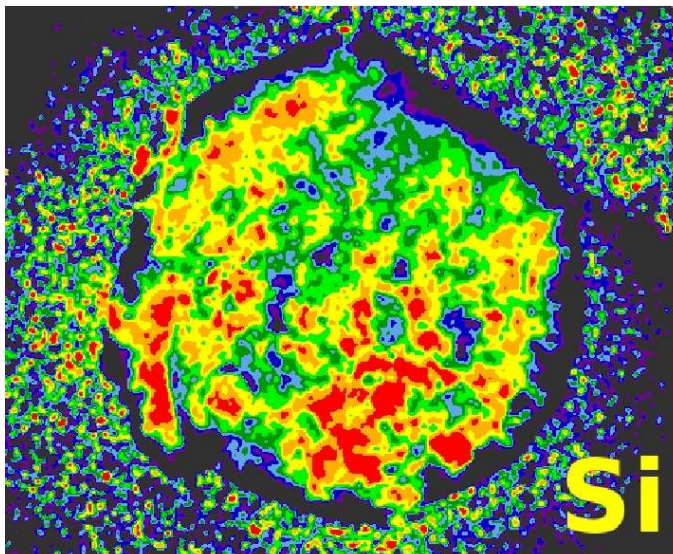


Fig. 8.— Equivalent-width map for Si. The excess of line emission in the southern hemisphere, an indication of an asymmetry in the ejecta distribution, is approximately 5% stronger than in the northern hemisphere.

width maps show the strength of the Si line at  $\sim 1.8$  keV relative to the strength of the underlying continuum emission and serves as a proxy for the amount of Si present in a given spatial region. We find that the spatial distribution is fairly uniform, with only a slight increase in the line strength (at the  $\sim 5\%$  level) in the southern portion of the remnant. This is consistent with a similar map shown in Hwang et al. (2002), which used the ACIS-S array and cut off the southernmost portion of the remnant. This is in contrast to what Winkler et al. (2014) found in SN 1006, where the Si was significantly stronger in the SE than in the NW.

Seitenzahl et al. (2013) explored various explosion models for Type Ia SNe. They compare three-dimensional hydrodynamical simulations for various delayed-detonation models for the first  $\sim 100$  seconds post-explosion. They calculate models with varying ignition conditions of the deflagration in the white dwarf at several values of the central density. Among the many outputs of these models are the velocity distributions of several elements, including Si. We do not, yet, have

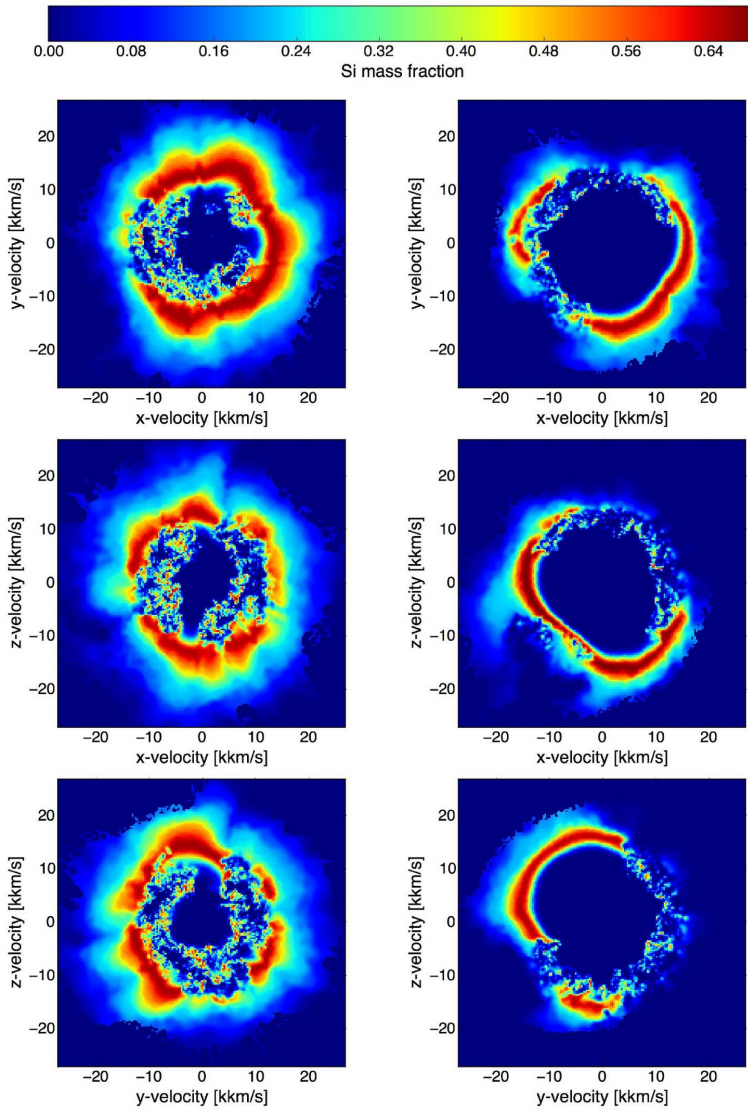


Fig. 9.— Slices through all three coordinate axis planes for the velocity distribution of Si shortly after the explosion. The N100 model of Seitzzahl et al. (2013) is shown on the left; the N5 model is on the right.

end-to-end simulations from the explosion of a supernova all the way to the supernova remnant phase hundreds of years later. Nonetheless, we can compare the velocity distribution that we see now to those produced in the explosion, as they are clearly connected during the ejecta-dominated

phase of the remnant.

In Figure 9, we show a comparison of velocities in all three coordinate planes for both the “N100” and “N5” models, where the numbers represent the number of ignition points within the white dwarf. We would like to emphasise here that the number of ignition sparks should not be taken literally. In the numerical simulations, the number and position of ignition sparks serves as a means to control the rate of fuel consumption (“deflagration strength”) and symmetry of the deflagration. For more discussion, see Sim et al. (2013). As can be seen from this figure and from those in Seitenzahl et al. (2013), models with more ignition kernels lead to more symmetric explosions, both in the spatial distribution of material and the velocity distribution. While we cannot conclusively select only one of the models that best fit the observational data, we conclude that the models with weakly ignited and asymmetric deflagrations, such as the “N3” and “N5” models, are disfavored for Tycho’s SNR.

One of the more notable features of Tycho is the presence of ejecta knots that protrude in front of the forward shock. These knots have been discussed by many authors before. Wang & Chevalier (2001) cite these knots as evidence of initial clumping in the ejecta, saying that they cannot be reproduced by fluid instabilities in a smooth ejecta profile in two-dimensional hydrodynamical simulations. Orlando et al. (2012) reached a similar conclusion using three-dimensional simulations regarding the necessity of clumping in the ejecta. By contrast, Warren & Blondin (2013) found that by varying the adiabatic index of the shocked gas,  $\gamma$ , their three-dimensional hydro simulations could reproduce the presence of ejecta knots ahead of the forward shock using smooth ejecta without any initial clumpiness. They concluded that clumpiness is not a necessary condition to explain the morphology of Tycho.

These and other previous studies focused on modeling the morphology of the remnant. We now have the ability to go one step further and compare the dynamics of Tycho with those from simulated data. We compare our observed spatial velocities with two hydrodynamical

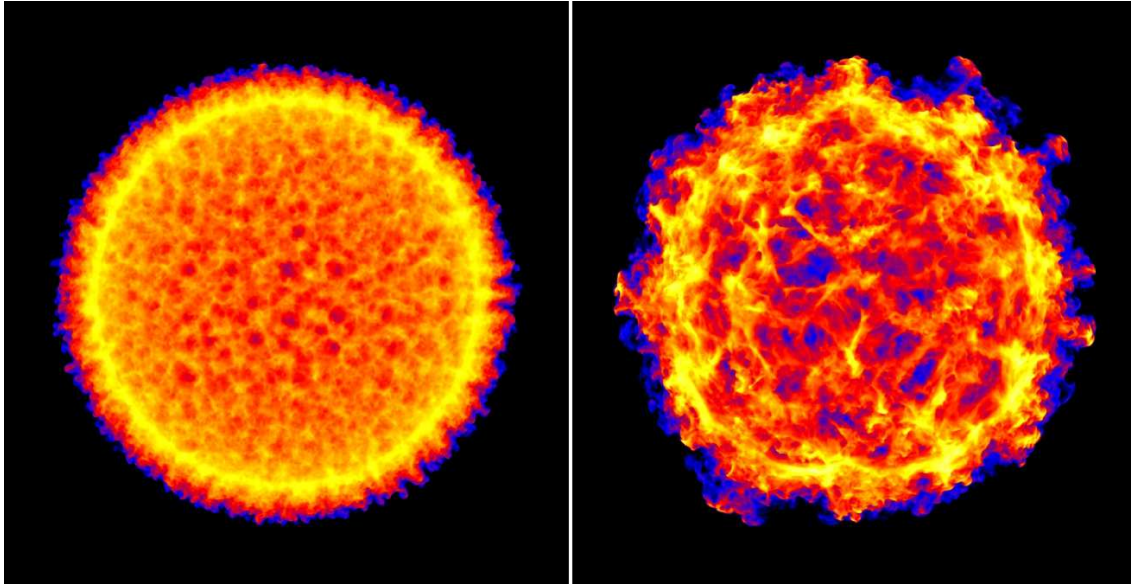


Fig. 10.— Hydrodynamical simulations of Tycho at the current epoch. These are two-dimensional projections of a three-dimensional simulation, described in the text. The model on the left has a smooth initial ejecta density profile; the one on the right consists of clumpy initial ejecta. The images are on the same spatial scale.

models: a smooth initial ejecta profile (which develops a "clumpy" structure over time due to fluid instabilities) and a clumpy initial profile. These simulations are described in detail in Warren & Blondin (2013); briefly, they use the hydrodynamics code VH-1 on a yin-yang spherical overset grid with 0.25 degree angular resolution. The model assumes the exponential density profile of Dwarkadas & Chevalier (1998) and “standard” explosion parameters of  $10^{51}$  ergs with  $1.4 M_{\odot}$  of ejecta. The clumpy model is produced using a Perlin algorithm (Perlin 1985) to generate noise with a maximum angular scale of  $\sim 20$  degrees and a maximum to minimum density contrast of 6.

Roughly a half-dozen knots protrude beyond Tycho’s forward shock. To remove the uncertainty in the absolute velocity caused by the unknown distance to Tycho, we use the dimensionless deceleration parameter,  $m (\equiv vt/R)$ , as our method of comparison. Here,  $v$  is the

proper motion (in arcseconds per year),  $t$  is the time since explosion, and  $R$  is the distance from the explosion site in arcseconds, which we assume to be the site determined in Paper II (slightly offset from the geometric center of the remnant). We compare motion only in the plane of the sky, as we cannot be certain of the radius of the knots in the Z-direction. We show the simulated images for both the smooth and clumpy models, showing only the reverse-shocked ejecta, in Figure 10.

As can be seen from Table 1, the  $m$  values vary throughout the remnant as measured from the *Chandra* images, from as low as  $\sim 0.3$  to as high as  $\sim 0.9$ , though the majority fall between 0.45-0.7. We measured the deceleration parameters for ejecta knots in both the smooth and clumpy models, finding a spread in values for the smooth model from  $\sim 0.4$  to 0.6 and for the clumpy model from  $\sim 0.5$  to 0.7. The dispersion in our measured values for Tycho is large enough to accommodate both models. We caution that care should be taken in comparing the observations to the models here, as we only have two hydrodynamic models. Large variations may exist between various clumpy ejecta models for supernova remnants.

Future work should further explore various ejecta distributions via multi-dimensional hydrodynamical simulations. For example, our work here only applies to the Si-rich ejecta, but Wang & Chevalier (2001) suggest that the level of clumpiness may differ between the Si and Fe-rich ejecta. Observationally, studies such as this are possible for other remnants, though the observational times required for *Chandra* are substantial. Future X-ray missions with substantially increased effective area will significantly reduce the observing time requirements, but we stress that for this type of science, this must be coupled with high-resolution imaging. Such missions would also allow this analysis to be done for other ejecta species. Ar, Ca, and Fe  $K\alpha$  are all present in Tycho, but are too faint to do using the existing *Chandra* observations. Finally, young remnants like Tycho should continue to be observed regularly with *Chandra*, since measurement uncertainties will decrease with time as the proper motions get larger.

## 5. Conclusions

Young supernova remnants offer a somewhat rare opportunity in astronomy: the chance to observe spatial evolution in real time. *Chandra* X-ray observations of Tycho’s supernova remnant spread out over 12 years constitute several percent of the lifetime of the remnant, enough to measure the expansion of the ejecta knots via their proper motion. Spectroscopic analysis yields the line-of-sight velocity, giving the first three-dimensional velocity map for the remnant of a Type Ia supernova.

We have nearly five dozen knots of ejecta for which we can reliably measure the proper motion in the plane of the sky and the red/blueshift of the spectral lines of Si and S. We find no measurable asymmetry in the velocity of the Si-rich ejecta in any direction. Some models of Type Ia SNe predict that such a velocity asymmetry should exist. When we compare our observations with the delayed detonation models of Seitenzahl et al. (2013), we favor models with strongly ignited, symmetric deflagrations, such as the N100 model.

We see very little spatial asymmetry when looking at the Si-rich ejecta. Equivalent-width maps of the  $\sim 1.8$  keV line of Si show that the Si is quite homogeneous. This is in contrast to some other young Type Ia remnants, such as SN 1006 and G1.9+0.3. The deceleration parameters we measure for the ejecta knots in the plane of the sky are consistent with hydrodynamical simulations of both smooth and clumpy ejecta profiles.

We thank Paul Plucinsky and R. Nick Durham at the *Chandra X-ray Center* for their assistance in quantifying the ACIS gain calibration for our spectral analysis. Support for this work was provided through Chandra Award GO4-15074Z issued by the Chandra X-ray Observatory Center, which is operated by the Smithsonian Astrophysical Observatory for and on behalf of NASA under contract NAS8-03060.

Table 1. Velocity Measurements for Ejecta Knots

Region	R.A.	Dec.	$\mu_X$	$\mu_Y$	$V_X$	$V_Y$	$V_Z$	$V_{Total}$	$m$
1	6.179	64.146	0.307 <sup>0.319</sup> <sub>0.294</sub>	0.014 <sup>0.015</sup> <sub>0.013</sub>	5090 <sup>5300</sup> <sub>4880</sub>	230 <sup>240</sup> <sub>220</sub>	620 <sup>780</sup> <sub>450</sub>	5140	0.56
2	6.181	64.161	0.301 <sup>0.310</sup> <sub>0.292</sub>	0.060 <sup>0.061</sup> <sub>0.058</sub>	4990 <sup>5140</sup> <sub>4840</sub>	990 <sup>1020</sup> <sub>960</sub>	710 <sup>990</sup> <sub>420</sub>	5140	0.54
3	6.187	64.158	0.320 <sup>0.356</sup> <sub>0.283</sub>	0.097 <sup>0.108</sup> <sub>0.086</sub>	5310 <sup>5910</sup> <sub>4700</sub>	1610 <sup>1800</sup> <sub>1430</sub>	1880 <sup>2230</sup> <sub>1510</sub>	5860	0.73
4	6.196	64.153	0.236 <sup>0.248</sup> <sub>0.223</sub>	0.066 <sup>0.070</sup> <sub>0.063</sub>	3910 <sup>4120</sup> <sub>3700</sub>	1100 <sup>1160</sup> <sub>1040</sub>	880 <sup>1130</sup> <sub>640</sub>	4160	0.41
5	6.198	64.128	0.256 <sup>0.278</sup> <sub>0.233</sub>	-0.108 <sup>-0.117</sup> <sub>-0.098</sub>	4240 <sup>4610</sup> <sub>3860</sub>	-1790 <sup>-1950</sup> <sub>-1630</sub>	1140 <sup>1360</sup> <sub>920</sub>	4740	0.38
6	6.201	64.107	0.240 <sup>0.257</sup> <sub>0.222</sub>	-0.152 <sup>-0.163</sup> <sub>-0.140</sub>	3990 <sup>4270</sup> <sub>3680</sub>	-2520 <sup>-2700</sup> <sub>-2330</sub>	-660 <sup>-810</sup> <sub>-520</sub>	4760	0.45
7	6.206	64.131	0.183 <sup>0.197</sup> <sub>0.169</sub>	-0.144 <sup>-0.155</sup> <sub>-0.132</sub>	3040 <sup>3280</sup> <sub>2800</sub>	-2380 <sup>-2570</sup> <sub>-2190</sub>	-640 <sup>-850</sup> <sub>-430</sub>	3920	0.56
8	6.212	64.154	0.205 <sup>0.219</sup> <sub>0.190</sub>	0.035 <sup>0.038</sup> <sub>0.033</sub>	3400 <sup>3640</sup> <sub>3160</sub>	590 <sup>630</sup> <sub>550</sub>	1790 <sup>1990</sup> <sub>1560</sub>	3890	0.45
9	6.215	64.110	0.260 <sup>0.270</sup> <sub>0.250</sub>	-0.094 <sup>-0.098</sup> <sub>-0.091</sub>	4320 <sup>4490</sup> <sub>4160</sub>	-1560 <sup>-1620</sup> <sub>-1500</sub>	-1870 <sup>-2170</sup> <sub>-1480</sub>	4960	0.55
10	6.218	64.139	0.210 <sup>0.229</sup> <sub>0.191</sub>	-0.038 <sup>-0.042</sup> <sub>-0.035</sub>	3480 <sup>3800</sup> <sub>3170</sub>	-630 <sup>-690</sup> <sub>-580</sub>	-420 <sup>-500</sup> <sub>-330</sub>	3560	0.47
11	6.222	64.106	0.202 <sup>0.214</sup> <sub>0.191</sub>	-0.161 <sup>-0.170</sup> <sub>-0.152</sub>	3360 <sup>3550</sup> <sub>3160</sub>	-2690 <sup>-2820</sup> <sub>-2510</sub>	-660 <sup>-780</sup> <sub>-530</sub>	4340	0.44
12	6.247	64.177	0.120 <sup>0.141</sup> <sub>0.101</sub>	0.132 <sup>0.155</sup> <sub>0.111</sub>	1990 <sup>2350</sup> <sub>1680</sub>	2190 <sup>2580</sup> <sub>1850</sub>	-1180 <sup>-1430</sup> <sub>-900</sub>	3190	0.29
13	6.248	64.085	0.175 <sup>0.210</sup> <sub>0.146</sub>	-0.224 <sup>-0.270</sup> <sub>-0.187</sub>	2900 <sup>3490</sup> <sub>2420</sub>	-3720 <sup>-4480</sup> <sub>-3110</sub>	1490 <sup>1830</sup> <sub>1310</sub>	4950	0.62
14	6.249	64.165	0.085 <sup>0.104</sup> <sub>0.065</sub>	0.108 <sup>0.131</sup> <sub>0.083</sub>	1410 <sup>1720</sup> <sub>1080</sub>	1790 <sup>2180</sup> <sub>1370</sub>	2600 <sup>2890</sup> <sub>2340</sub>	3460	0.33
15	6.253	64.109	0.185 <sup>0.194</sup> <sub>0.175</sub>	-0.138 <sup>-0.145</sup> <sub>-0.131</sub>	3060 <sup>3220</sup> <sub>2900</sub>	-2290 <sup>-2410</sup> <sub>-2170</sub>	2120 <sup>2400</sup> <sub>1840</sub>	4370	0.62
16	6.260	64.139	0.135 <sup>0.160</sup> <sub>0.108</sub>	0.003 <sup>0.004</sup> <sub>0.002</sub>	2240 <sup>2660</sup> <sub>1800</sub>	50 <sup>60</sup> <sub>40</sub>	770 <sup>1130</sup> <sub>420</sub>	2370	0.43
17	6.262	64.137	0.118 <sup>0.144</sup> <sub>0.090</sub>	-0.020 <sup>-0.025</sup> <sub>-0.016</sub>	1950 <sup>2390</sup> <sub>1500</sub>	-340 <sup>-410</sup> <sub>-260</sub>	2950 <sup>3180</sup> <sub>2700</sub>	3560	0.37
18	6.268	64.131	0.114 <sup>0.155</sup> <sub>0.128</sub>	0.179 <sup>0.207</sup> <sub>0.149</sub>	1890 <sup>2190</sup> <sub>1580</sub>	2970 <sup>3430</sup> <sub>2480</sub>	-1930 <sup>-2170</sup> <sub>-1680</sub>	4020	0.44
19	6.274	64.130	0.141 <sup>0.155</sup> <sub>0.128</sub>	-0.050 <sup>-0.054</sup> <sub>-0.045</sub>	2350 <sup>2570</sup> <sub>2130</sub>	-820 <sup>-900</sup> <sub>-740</sub>	-1110 <sup>-1290</sup> <sub>-930</sub>	2730	0.58
20	6.281	64.070	0.070 <sup>0.071</sup> <sub>0.068</sub>	-0.358 <sup>-0.367</sup> <sub>-0.347</sub>	1150 <sup>1190</sup> <sub>1120</sub>	-5930 <sup>-6090</sup> <sub>-5760</sub>	-1060 <sup>-1280</sup> <sub>-850</sub>	6140	0.58
21	6.282	64.170	0.055 <sup>0.060</sup> <sub>0.049</sub>	0.117 <sup>0.128</sup> <sub>0.106</sub>	910 <sup>990</sup> <sub>820</sub>	1950 <sup>2120</sup> <sub>1760</sub>	-2150 <sup>-2940</sup> <sub>-1730</sub>	3040	0.41
22	6.294	64.067	0.028 <sup>0.028</sup> <sub>0.027</sub>	-0.369 <sup>-0.379</sup> <sub>-0.360</sub>	460 <sup>470</sup> <sub>450</sub>	-6130 <sup>-6280</sup> <sub>-5970</sub>	-920 <sup>-1070</sup> <sub>-770</sub>	6220	0.58
23	6.294	64.095	0.003 <sup>0.005</sup> <sub>0.002</sub>	-0.095 <sup>-0.128</sup> <sub>-0.064</sub>	60 <sup>80</sup> <sub>40</sub>	-1580 <sup>-2130</sup> <sub>-1060</sub>	2130 <sup>2330</sup> <sub>1940</sub>	2660	0.81
24*	6.294	64.197	0.037 <sup>0.040</sup> <sub>0.034</sub>	0.169 <sup>0.181</sup> <sub>0.157</sub>	620 <sup>660</sup> <sub>570</sub>	2800 <sup>3000</sup> <sub>2600</sub>	3190 <sup>3390</sup> <sub>2790</sub>	4290	0.46
25	6.299	64.082	0.073 <sup>0.077</sup> <sub>0.069</sub>	-0.243 <sup>-0.256</sup> <sub>-0.230</sub>	1210 <sup>1270</sup> <sub>1150</sub>	-4040 <sup>-4240</sup> <sub>-3820</sub>	-320 <sup>-490</sup> <sub>-130</sub>	4230	0.64

Table 1—Continued

Region	R.A.	Dec.	$\mu_X$	$\mu_Y$	$V_X$	$V_Y$	$V_Z$	$V_{Total}$	$m$
26*	6.299	64.192	0.011 <sup>0.013</sup> <sub>0.008</sub>	0.158 <sup>0.186</sup> <sub>0.117</sub>	180 <sup>210</sup> <sub>130</sub>	2610 <sup>3090</sup> <sub>1950</sub>	-880 <sup>-1140</sup> <sub>-610</sub>	2760	0.27
27*	6.307	64.198	-0.005 <sup>-0.006</sup> <sub>-0.005</sub>	0.246 <sup>0.263</sup> <sub>0.228</sub>	-90 <sup>-90</sup> <sub>-80</sub>	4080 <sup>4370</sup> <sub>3780</sub>	1950 <sup>2250</sup> <sub>1650</sub>	4520	0.62
28	6.318	64.169	0.018 <sup>0.019</sup> <sub>0.016</sub>	0.179 <sup>0.192</sup> <sub>0.166</sub>	290 <sup>310</sup> <sub>270</sub>	2970 <sup>3180</sup> <sub>2760</sub>	3360 <sup>3660</sup> <sub>2570</sub>	4490	0.71
29	6.322	64.180	-0.007 <sup>-0.009</sup> <sub>-0.006</sub>	0.153 <sup>0.177</sup> <sub>0.128</sub>	-120 <sup>-140</sup> <sub>-100</sub>	2540 <sup>2940</sup> <sub>2130</sub>	-1380 <sup>-1640</sup> <sub>-1130</sub>	2890	0.45
30*	6.327	64.213	0.005 <sup>0.005</sup> <sub>0.005</sub>	0.393 <sup>0.402</sup> <sub>0.383</sub>	80 <sup>80</sup> <sub>80</sub>	6520 <sup>6670</sup> <sub>6360</sub>	770 <sup>1540</sup> <sub>90</sub>	6560	0.62
31	6.329	64.187	-0.027 <sup>-0.031</sup> <sub>-0.024</sub>	0.161 <sup>0.182</sup> <sub>0.139</sub>	-450 <sup>-510</sup> <sub>-390</sub>	2680 <sup>3020</sup> <sub>2310</sub>	-2630 <sup>-2990</sup> <sub>-2260</sub>	3780	0.44
32	6.342	64.074	-0.026 <sup>-0.027</sup> <sub>-0.025</sub>	-0.292 <sup>-0.303</sup> <sub>-0.281</sub>	-430 <sup>-450</sup> <sub>-420</sub>	-4840 <sup>-5030</sup> <sub>4660</sub>	410 <sup>620</sup> <sub>200</sub>	4880	0.52
33	6.344	64.087	-0.032 <sup>-0.036</sup> <sub>-0.029</sub>	-0.233 <sup>-0.257</sup> <sub>-0.210</sub>	-540 <sup>-590</sup> <sub>-480</sub>	-3870 <sup>-4270</sup> <sub>-3480</sub>	-1120 <sup>-1300</sup> <sub>-950</sub>	4070	0.57
34	6.344	64.095	-0.053 <sup>-0.060</sup> <sub>-0.046</sub>	-0.202 <sup>-0.229</sup> <sub>-0.177</sub>	-870 <sup>-990</sup> <sub>-770</sub>	-3350 <sup>-3800</sup> <sub>-2940</sub>	1920 <sup>2190</sup> <sub>1630</sub>	3960	0.62
35	6.360	64.198	-0.058 <sup>-0.062</sup> <sub>-0.054</sub>	0.310 <sup>0.319</sup> <sub>0.291</sub>	-960 <sup>-1030</sup> <sub>-900</sub>	5140 <sup>5480</sup> <sub>4820</sub>	1140 <sup>1380</sup> <sub>910</sub>	5360	0.82
36	6.370	64.114	-0.084 <sup>-0.093</sup> <sub>-0.076</sub>	-0.108 <sup>-0.118</sup> <sub>-0.097</sub>	-1400 <sup>-1540</sup> <sub>-1260</sub>	-1790 <sup>-1970</sup> <sub>-1610</sub>	-1310 <sup>-1540</sup> <sub>-1060</sub>	2620	0.68
37	6.371	64.195	-0.097 <sup>-0.102</sup> <sub>-0.093</sub>	0.305 <sup>0.319</sup> <sub>0.291</sub>	-1620 <sup>-1690</sup> <sub>-1540</sub>	5060 <sup>5290</sup> <sub>4830</sub>	2030 <sup>2260</sup> <sub>1810</sub>	5690	0.71
38	6.375	64.177	-0.119 <sup>-0.128</sup> <sub>-0.111</sub>	0.146 <sup>0.157</sup> <sub>0.136</sub>	-1980 <sup>-2120</sup> <sub>-1850</sub>	2430 <sup>2610</sup> <sub>2260</sub>	2040 <sup>2310</sup> <sub>1770</sub>	3740	0.50
39	6.396	64.088	-0.145 <sup>-0.152</sup> <sub>-0.138</sub>	-0.246 <sup>-0.258</sup> <sub>-0.234</sub>	-2410 <sup>-2530</sup> <sub>-2290</sub>	-4080 <sup>-4290</sup> <sub>-3880</sub>	1000 <sup>1370</sup> <sub>690</sub>	4840	0.67
40	6.399	64.173	-0.182 <sup>-0.197</sup> <sub>-0.168</sub>	0.100 <sup>0.108</sup> <sub>0.092</sub>	-3030 <sup>-3270</sup> <sub>-2780</sub>	1660 <sup>1800</sup> <sub>1530</sub>	-1410 <sup>-1600</sup> <sub>-1210</sub>	3730	0.63
41	6.400	64.165	-0.201 <sup>-0.218</sup> <sub>-0.183</sub>	0.080 <sup>0.087</sup> <sub>0.073</sub>	-3330 <sup>-3610</sup> <sub>-3040</sub>	1330 <sup>1440</sup> <sub>1210</sub>	-2630 <sup>-2890</sup> <sub>-2370</sub>	4450	0.94
42	6.403	64.193	-0.088 <sup>-0.094</sup> <sub>-0.082</sub>	0.263 <sup>0.281</sup> <sub>0.244</sub>	-1460 <sup>-1560</sup> <sub>-1360</sub>	4370 <sup>4660</sup> <sub>4060</sub>	-310 <sup>-460</sup> <sub>-160</sub>	4620	0.48
43	6.422	64.186	-0.158 <sup>-0.165</sup> <sub>-0.152</sub>	0.128 <sup>0.133</sup> <sub>0.123</sub>	-2620 <sup>-2740</sup> <sub>-2520</sub>	2120 <sup>2210</sup> <sub>2030</sub>	1000 <sup>1130</sup> <sub>880</sub>	3520	0.58
44	6.431	64.107	-0.292 <sup>-0.309</sup> <sub>-0.273</sub>	-0.058 <sup>-0.061</sup> <sub>-0.054</sub>	-4840 <sup>-5120</sup> <sub>-4530</sub>	-960 <sup>-1010</sup> <sub>-900</sub>	-1380 <sup>-1850</sup> <sub>-1050</sub>	5120	0.65
45	6.433	64.176	-0.242 <sup>-0.262</sup> <sub>-0.220</sub>	0.133 <sup>0.144</sup> <sub>0.121</sub>	-4010 <sup>-4350</sup> <sub>-3660</sub>	2200 <sup>2390</sup> <sub>2010</sub>	680 <sup>940</sup> <sub>430</sub>	4620	0.43
46	6.434	64.161	-0.165 <sup>-0.175</sup> <sub>-0.156</sub>	0.126 <sup>0.134</sup> <sub>0.119</sub>	-2740 <sup>-2900</sup> <sub>-2590</sub>	2100 <sup>2220</sup> <sub>1980</sub>	-1260 <sup>-1390</sup> <sub>-1120</sub>	3680	0.84
47	6.447	64.188	-0.186 <sup>-0.191</sup> <sub>-0.182</sub>	0.164 <sup>0.168</sup> <sub>0.160</sub>	-3080 <sup>-3160</sup> <sub>-3020</sub>	2720 <sup>2790</sup> <sub>2660</sub>	480 <sup>630</sup> <sub>320</sub>	4140	0.55
48	6.452	64.178	-0.273 <sup>-0.282</sup> <sub>-0.264</sub>	0.162 <sup>0.168</sup> <sub>0.157</sub>	-4540 <sup>-4680</sup> <sub>-4380</sub>	2690 <sup>2780</sup> <sub>2600</sub>	640 <sup>790</sup> <sub>500</sub>	5310	0.62
49	6.463	64.146	-0.214 <sup>-0.235</sup> <sub>-0.193</sub>	-0.018 <sup>-0.019</sup> <sub>-0.016</sub>	-3560 <sup>-3890</sup> <sub>-3200</sub>	-290 <sup>-320</sup> <sub>-260</sub>	-1040 <sup>-1330</sup> <sub>-740</sub>	3720	0.61
50	6.465	64.095	-0.254 <sup>-0.264</sup> <sub>-0.245</sub>	-0.223 <sup>-0.231</sup> <sub>-0.214</sub>	-4220 <sup>-4380</sup> <sub>-4070</sub>	-3700 <sup>-3830</sup> <sub>-3560</sub>	1730 <sup>1910</sup> <sub>1500</sub>	5870	0.75

Table 1—Continued

Region	R.A.	Dec.	$\mu_X$	$\mu_Y$	$V_X$	$V_Y$	$V_Z$	$V_{Total}$	$m$
51	6.471	64.162	$-0.228_{-0.223}^{-0.233}$	$0.152_{0.148}^{0.155}$	$-3780_{-3710}^{-3860}$	$2510_{2460}^{2570}$	$390_{100}^{690}$	4560	0.61
52	6.471	64.173	$-0.246_{-0.240}^{-0.252}$	$0.127_{0.123}^{0.130}$	$-4090_{-3980}^{-4190}$	$2100_{2040}^{2150}$	$610_{410}^{810}$	4630	0.56
53	6.476	64.136	$-0.317_{-0.311}^{-0.323}$	$0.023_{0.023}^{0.024}$	$-5260_{-5170}^{-5350}$	$390_{380}^{390}$	$-980_{-550}^{-1430}$	5360	0.65
54	6.477	64.104	$-0.304_{-0.296}^{-0.310}$	$-0.185_{-0.181}^{-0.189}$	$-5040_{-4910}^{-5150}$	$-3070_{-3000}^{-3140}$	$880_{230}^{1500}$	5970	0.72
55	6.489	64.126	$-0.330_{-0.327}^{-0.335}$	$-0.040_{-0.040}^{-0.041}$	$-5480_{-5420}^{-5560}$	$-660_{-660}^{-670}$	$-2460_{-2290}^{-2610}$	6040	0.64
56	6.490	64.131	$-0.279_{-0.273}^{-0.284}$	$0.076_{0.074}^{0.077}$	$-4620_{-4530}^{-4710}$	$1260_{1230}^{1280}$	$-1390_{-1190}^{-1600}$	4990	0.48
57	6.492	64.112	$-0.360_{-0.354}^{-0.367}$	$-0.079_{-0.077}^{-0.080}$	$-5980_{-5880}^{-6090}$	$-1300_{-1280}^{-1330}$	$-1600_{-1200}^{-2130}$	6320	0.62

Note. — Region number corresponds to numbers shown on Figure 1. Regions are numbered in order of ascending right ascension, and were drawn on the 2009 observation. R.A. and Dec. are given in decimal degrees in J2000 coordinates. All velocities given in  $\text{km s}^{-1}$  and rounded to the nearest  $10 \text{ km s}^{-1}$ . X is positive to the west, Y is positive to the north, and Z is positive away from the observer. Uncertainties are statistical only. Systematic uncertainties due to WCS alignment for  $V_X$  and  $V_Y$  are negligible. Systematic uncertainties for  $V_Z$  due to CCD gain calibration are  $900 \text{ km s}^{-1}$  for all regions except those with an asterisk, where the systematic uncertainties are  $3000 \text{ km s}^{-1}$ . Deceleration parameter,  $m$ , is described in the text and only measured in the plane of the sky, assuming the calculated explosion center determined in Paper II of  $\alpha = 0^h 25^m 22.6^s$  and  $\delta = 64^\circ 8' 32.7''$ .

Table 2. XSPEC NEI Model Fits to Ejecta Knot Spectra

Region	$\tau_i$ ( $10^{10} \text{ cm}^{-3} \text{ s}$ )	kT (keV)	$\chi^2/\text{d.o.f.}$
1	5.36	1.23	135/99
2	2.12	1.89	139/99
3	6.29	1.26	97/98
4	6.54	1.13	128/94
5	1.96	1.54	153/100
6	4.29	1.56	124/99
7	4.41	1.65	189/106
8	6.51	1.39	188/99
9	5.13	1.43	110/93
10	8.56	1.17	217/103
11	7.57	1.10	225/105
12	2.63	2.61	165/100
13	5.09	1.35	149/94
14	11.0	1.35	149/94
15	13.2	0.94	114/92
16	5.76	1.37	107/92
17	8.01	1.20	185/96
18	6.91	1.11	158/98
19	19.2	0.83	252/93
20	5.11	1.15	104/93
21	3.98	1.13	100/93
22	4.31	1.29	103/98
23	8.29	1.12	204/98
24	7.83	1.50	151/102
25	12.7	0.88	145/100

Table 2—Continued

Region	$\tau_i$ ( $10^{10} \text{ cm}^{-3} \text{ s}$ )	kT (keV)	$\chi^2/\text{d.o.f.}$
26	3.92	2.36	159/101
27	9.97	1.21	238/101
28	5.27	1.21	135/93
29	6.68	1.26	95/96
30	5.05	2.28	70/73
31	5.80	1.39	108/96
32	4.93	1.20	97/98
33	11.4	0.90	123/93
34	18.7	0.88	205/93
35	6.22	1.24	159/98
36	6.87	1.12	108/95
37	8.18	1.19	147/99
38	25.8	0.84	181/104
39	2.23	2.10	109/100
40	10.1	1.03	163/96
41	8.98	0.95	96/95
42	5.48	1.42	144/100
43	9.79	1.06	244/100
44	8.64	0.98	99/84
45	4.90	1.51	113/94
46	7.76	1.11	119/98
47	8.12	1.05	157/98
48	9.04	0.98	148/98
49	13.5	0.93	129/90
50	5.59	1.20	141/100

Table 2—Continued

Region	$\tau_i$ ( $10^{10}$ cm $^{-3}$ s)	kT (keV)	$\chi^2$ /d.o.f.
51	4.72	1.36	76/92
52	6.95	1.02	163/94
53	8.35	1.04	123/100
54	104	0.57	102/100
55	4.45	1.47	310/100
56	4.94	1.38	119/90
57	8.43	0.86	204/80

Note. —  $\tau_i$  is ionization timescale, the integral of electron density over time in the post-shock gas.

## REFERENCES

- Albinson, J.S., Tuffs, R.J., Swinbank, E., & Gull, S.F. 1986, *MNRAS*, 219, 427
- Baade, W. 1945, *ApJ*, 102, 309
- Badenes, C., Borkowski, K.J., Hughes, J.P., Hwang, U., & Bravo, E. 2006, *ApJ*, 645, 1373
- Borkowski, K.J. et al. 2013, *ApJ*, 771, 9
- Borkowski, K.J., Gwynne, P., Reynolds, S.P., Green, D.A., Hwang, U., Petre, R., & Willett, R.,  
2017, accepted
- Cassam-Chenaï, G., Hughes, J.P., Ballet, J., & Decourchelle, A. 2007, *ApJ*, 665, 315
- Chevalier, R.A., Kirshner, R.P., & Raymond, J.C. 1980, *ApJ*, 235, 186
- Delaney, T., et al. 2010, *ApJ*, 725, 2038
- Dwarkadas, V.V. & Chevalier, R.A. 1998, *ApJ*, 497, 807
- Fesen, R.A., et al. 2006, *ApJ*, 645, 283
- Furuzawa, A., et al. 2009, *ApJ*, 693, 61
- Hayato, A., et al. 2010, *ApJ*, 725, 894
- Hughes, J.P. 2000, *ApJ*, 545, 53
- Hwang, U., Decourchelle, A., Holt, S., Petre, R. 2002, *ApJ*, 581, 1101
- Katsuda, S., Tsunemi, H., & Mori, K. 2008, *ApJ*, 678, 35
- Katsuda, S., Petre, R., Hughes, J.P., Hwang, U., Yamaguchi, H., Hayato, A., Mori, K., Tsunemi,  
H. 2010, *ApJ*, 709, 1387

Kerzendorf, W.E., et al. 2013, ApJ, 774, 99

Krause, O., Tanaka, M., Usuda, T., Hattori, T., Goto, M., Birkmann, S., & Nomoto, K. 2008,  
*Nature*, 456, 617

Maeda, K., et al. 2010, *Nature*, 466, 82

Motohara, K., et al. 2006, ApJ, 652, 101

Orlando, S., Bocchino, F., Miceli, M., Petruk, O., & Pumo, M.L. 2012, ApJ, 749, 156

Perlin, K. 1985, SIGGRAPH Comput. Graph. 19, 287

Ressler, S.M., Katsuda, S., Reynolds, S.P., Long, K.S., Petre, R., Williams, B.J., & Winkler, P.F.  
2014, ApJ, 790, 85

Rest, A., et al. 2008, ApJ, 681, 81

Reynolds, S.P. & Keohane, J.W. 1999, ApJ, 525, 368

Reynoso, E.M., Moffett, D.A., Goss, W.M., Dubner, G.M., Dickel, J.R., Reynolds, S.P., &  
Giacani, E.B. 1997, ApJ, 491, 816

Ruiz-Lapuente, P., et al. 2004, *Nature*, 431, 1069

Sato, T. & Hughes, J.P., arXiv:1605.09059

Schaefer, B.E. & Pagnotta, A. 2012, *Nature*, 481, 164

Schwarz, U.J., Goss, W.M., Kalberla, P.M., & Benaglia, P. 1995, A&A, 299, 193

Seitzzahl, I.R., et al. 2013, MNRAS, 429, 1156

Sim, S.A., et al. 2013, MNRAS, 436, 333

Stephenson, F.R. & Green, D.A. 2002, *Historical Supernovae and their Remnants*, Oxford University Press

Tran, A., Williams, B.J., Petre, R., Ressler, S.M., & Reynolds, S.P. 2015, *ApJ*, 812, 101

Wang, C.-H. & Chevalier, R.A. 2001, *ApJ*, 549, 1119

Wang, L. & Wheeler, J.C. 2008, *ARA&A*, 46, 433

Warren, J.S., et al. 2005, *ApJ*, 634, 376

Warren, D.C. & Blondin, J.M. 2013, *MNRAS*, 429, 3099

Webbink, R.F. 1984, *ApJ*, 277, 355

Whelan, J., & Iben, I., Jr. 1973, *ApJ*, 186, 1007

Williams, B.J., et al. 2013, *ApJ*, 770, 129

Williams, B.J., et al. 2016, *ApJL*, 823, 32

Winkler, P.F., et al. 2014, *ApJ*, 781, 65

Xue, Z. & Schaefer, B.E. 2015, *ApJ*, 809, 183

Yamaguchi, H., Katsuda, S., & Castro, D. et al. 2016, *ApJ*, 820, 3

Yamaguchi, H., Hughes, J.P., Badenes, C., Bravo, E., Seitenzahl, I.R., Martinez-Rodriguez, H., Park, S., & Petre, R. 2017, *ApJ*, 834, 124